

Polygonal finite elements for finite elasticity

Heng Chi, Cameron Talischi, Oscar Lopez-Pamies and Glaucio H. Paulino^{*,†}

Department of Civil and Environmental Engineering, University of Illinois at Urbana-Champaign, 205 North Mathews Ave., Urbana, IL 61801, USA

SUMMARY

Nonlinear elastic materials are of great engineering interest, but challenging to model with standard finite elements. The challenges arise because nonlinear elastic materials are characterized by non-convex stored-energy functions as a result of their ability to undergo large reversible deformations, are incompressible or nearly incompressible, and often times possess complex microstructures. In this work, we propose and explore an alternative approach to model finite elasticity problems in two dimensions by using polygonal discretizations. We present both lower order displacement-based and mixed polygonal finite element approximations, the latter of which consist of a piecewise constant pressure field and a linearly-complete displacement field at the element level. Through numerical studies, the mixed polygonal finite elements are shown to be stable and convergent. For demonstration purposes, we deploy the proposed polygonal discretization to study the nonlinear elastic response of rubber filled with random and periodic distributions of rigid particles, as well as the development of cavitation instabilities in elastomers containing vacuous defects. These physically-based examples illustrate the potential of polygonal finite elements in studying and modeling nonlinear elastic materials with complex microstructures under finite deformations. Copyright © 2014 John Wiley & Sons, Ltd.

Received 7 June 2014; Revised 3 September 2014; Accepted 5 September 2014

KEY WORDS: polygonal finite elements; finite elasticity; incompressibility; mixed variational principle; filled elastomers; cavitation

1. INTRODUCTION

Many organic materials are characterized by their ability to undergo large reversible deformations in response to a variety of stimuli, including mechanical forces, electric and magnetic fields, and temperature changes. While they have long been utilized in numerous engineering applications, modern advances in material science have demonstrated that soft organic materials, such as electro-active and magneto-active elastomers, gels, and shape-memory polymers, hold tremendous potential to enable new technologies essentially as the new generation of sensors and actuators. From a mechanical perspective, most of these materials, as complex as they are, can be approximated ‘simply’ as nonlinear elastic. They are also, more often than not, highly heterogeneous possessing complex microstructures. Thus, while nonlinear elastic, the underlying local deformations in soft organic materials are exceptionally complex.

Computational microscopic studies of nonlinear elastic materials, especially those with complex microstructures, to gain quantitative understanding of their complex behavior are essential in guiding their optimization and actual use in technological applications. The standard finite element approach, however, has been shown to be inadequate in simulating processes involving realistic large deformations. A simple but glaring example can be found in the study of filled elastomers. Experimentally, a synthetic rubber filled with 20% volume fraction of randomly distributed silica particles can be stretched more than four times its original length without any internal damage under

^{*}Correspondence to: Glaucio H. Paulino, Department of Civil and Environmental Engineering, University of Illinois at Urbana-Champaign, 205 North Ave., Urbana, IL 61801, USA.

[†]E-mail: paulino@uiuc.edu

uniaxial tension [1]. By contrast, a finite element model, based on standard 10-node hybrid elements with linear pressure, is only able to deform to a macroscopic stretch of $\lambda = 1.5$ [2]. This is because there are a number of matrix regions squeezed in between particles where the local deformations are very large (involving stretches of up to five in this example) and convergence cannot be reached [2]. The use of different elements types, meshes, and remeshing has been shown to be inefficient, or of little help, to circumvent this problem [2, 3]. Motivated by the aforementioned limitations of the standard finite element method (FEM), in this paper, we propose a framework using polygonal finite elements as an alternative approach to study nonlinear elastic materials.

Despite its relatively long history of development, dating back to the work of Wachspress [4], the numerical implementation and application of polygonal finite elements in engineering problems are more recent [5–10]. Polygonal finite elements have shown to possess advantages over the classical finite elements, that is, triangular and quadrilateral elements, in many aspects. From a geometric point of view, it offers more flexibility in discretization. Making use of the concept of Voronoi tessellation, a number of meshing algorithms for polygonal meshes have been developed that allow the meshing of arbitrary geometries [11–13]. In addition, because there is no restriction on the number of sides in polygonal finite element, polygonal elements or n -gons ($n = 3, 4, 5 \dots$) can be useful in mesh transitions and refinement. Representative examples can be found in the fracture literature, where the use of polygonal finite elements makes possible local modifications, such as element splitting and adaptive refinement techniques, to better capture the propagation of cracks and crack branching [14, 15]. In addition to their advantages in mesh generation and refinement, polygonal finite elements can outperform their triangular and quadrilateral counterparts under bending and shear loadings [8]. From an analysis point of view, when incompressible or nearly incompressible materials are considered, mixed finite elements are typically employed, for which numerical stability is a critical issue [16, 17]. Unfortunately, it turns out that many choices of mixed finite elements are numerically unstable [18, 19]. For example, coupled with piecewise constant pressure approximations, linear interpolations of the displacement field on triangular meshes generally exhibit locking behavior, while bi-linear interpolations of the displacement field on quadrilateral meshes may lead to spurious pressure modes. By contrast, the approximation of the displacement field by linearly-complete barycentric coordinates with piecewise constant pressure interpolation on Voronoi-type meshes has been shown to be unconditionally stable without the need of any additional treatments [10].

Polygonal finite elements have been extensively studied within the context of linear problems. That is not the case for nonlinear problems (see, however, [20, 21] for some recent work on elastoplasticity). In this paper, both displacement-based and mixed polygonal finite elements are extended and formulated for finite elasticity problems. For demonstration purposes, they are utilized to study three types of physically-based problems: the nonlinear elastic response of rubber filled (1) with a random distribution of circular rigid particles and (2) with a periodic distribution of elliptical rigid particles, and (3) the development of cavitation instabilities in elastomers containing vacuous defects. These applications serve to distinctly illustrate that polygonal elements are particularly well suited to model particulate microstructures, incorporate periodic boundary conditions, and bridge different length scales. They also appear to be more tolerant to accommodate large local deformations than classic triangular and quadrilateral elements, while at the same time are more accurate and numerically stable.

The paper is organized as follows. In Section 2, both displacement-based and two-field mixed variational principles are presented in a continuum setting. Their finite element approximations on polygonal meshes and the implementation aspects are then discussed in Section 3. In Section 4, through numerical studies, the stability and convergence of the polygonal finite elements are verified. Section 5 deals with the applications of the polygonal finite elements to filled rubber and cavitation instabilities. Finally, we provide some concluding remarks in Section 6.

2. FINITE ELASTICITY FORMULATIONS

In this section, we recall the equations of elastostatics specialized to the case of hyperelastic materials. Three variational formulations are presented: (1) the standard displacement-based formulation

[22–24]; (2) a general mixed formulation involving the displacement field and a pressure-like scalar field as the trial fields; and (3) the commonly adopted two-field mixed variational in the finite element literature based on the multiplicative splitting of the deformation gradient tensor [25–29].

2.1. Displacement-based formulation

Consider a body that occupies a domain Ω , with boundary $\partial\Omega$, in its undeformed stress-free configuration. The constitutive behavior of the body is characterized by the stored-energy function W , which is taken to be a non-negative, objective, non-convex function of the deformation gradient $\mathbf{F} = \nabla\mathbf{u} + \mathbf{I}$, where \mathbf{u} denotes the displacement field, \mathbf{I} stands for the identity in the space of second-order tensors, and ∇ is the gradient operator with respect to undeformed configuration. In terms of \mathbf{F} , the first Piola–Kirchhoff stress tensor \mathbf{P} at each material point $\mathbf{X} \in \Omega$ is given by

$$\mathbf{P}(\mathbf{X}) = \frac{\partial W}{\partial \mathbf{F}}(\mathbf{X}, \mathbf{F}(\mathbf{u})). \quad (1)$$

The body is assumed to be subjected to a prescribed displacement field \mathbf{u}^0 on $\Gamma_{\mathbf{u}}$ and to a prescribed surface traction \mathbf{t}^0 (per unit undeformed area) on $\Gamma_{\mathbf{t}}$, where $\partial\Omega = \Gamma_{\mathbf{u}} \cup \Gamma_{\mathbf{t}}$ and $\Gamma_{\mathbf{u}} \cap \Gamma_{\mathbf{t}} = \emptyset$. It is also assumed to be subjected to a body force \mathbf{f} (per unit undeformed volume) over Ω . It then follows from the classical principle of minimum potential energy that the equilibrium displacement field \mathbf{u} minimizes the potential energy Π among the displacement fields that are kinematically admissible:

$$\Pi(\mathbf{u}) = \min_{\mathbf{v} \in \mathcal{K}} \Pi(\mathbf{v}), \quad (2)$$

with

$$\Pi(\mathbf{v}) = \int_{\Omega} W(\mathbf{X}, \mathbf{F}(\mathbf{v})) d\mathbf{X} - \int_{\Omega} \mathbf{f} \cdot \mathbf{v} d\mathbf{X} - \int_{\Gamma_{\mathbf{t}}} \mathbf{t}^0 \cdot \mathbf{v} dS. \quad (3)$$

In the aforementioned expression, \mathcal{K} stands for a sufficiently large set of displacements such that $\mathbf{v} = \mathbf{u}^0$ on $\Gamma_{\mathbf{u}}$.

The weak form of the Euler–Lagrange equations associated with the variational problem (2) reads as follows:

$$G(\mathbf{u}, \mathbf{v}) = D\Pi(\mathbf{u}) \cdot \mathbf{v} = \int_{\Omega} \frac{\partial W}{\partial \mathbf{F}}(\mathbf{X}, \mathbf{F}(\mathbf{u})) : \nabla \mathbf{v} d\mathbf{X} - \int_{\Omega} \mathbf{f} \cdot \mathbf{v} d\mathbf{X} - \int_{\Gamma_{\mathbf{t}}} \mathbf{t}^0 \cdot \mathbf{v} dS = 0 \quad \forall \mathbf{v} \in \mathcal{K}_0, \quad (4)$$

where \mathcal{K}_0 denotes the set of all kinematically admissible displacement fields that vanish on $\Gamma_{\mathbf{u}}$. For use in typical solvers within the finite element analysis of Equation (4), such as the Newton–Raphson method, it is expedient to record its linearization. Assuming that all external loads are deformation independent, the result reads as

$$G(\mathbf{u}, \mathbf{v}) + DG(\mathbf{u}, \mathbf{v}) \cdot \mathbf{w} = 0 \quad \forall \mathbf{v} \in \mathcal{K}_0, \quad (5)$$

with

$$DG(\mathbf{u}, \mathbf{v}) \cdot \mathbf{w} = \int_{\Omega} \nabla \mathbf{v} : \frac{\partial^2 W}{\partial \mathbf{F}^2}(\mathbf{X}, \mathbf{F}(\mathbf{u})) : \nabla \mathbf{w} d\mathbf{X}, \quad (6)$$

where \mathbf{w} is the incremental displacement field.

2.2. A general two-field mixed variational formulation

For nonlinear elastic materials that are nearly incompressible, the variational principle in (2)–(3) is known to perform poorly in standard FEMs. This phenomenon is usually referred to as volumetric

locking [19]. As a standard remedy, mixed variational principles, which involve not only deformation but also stress fields, are utilized instead [30, 31]. The mixed variational principle within this class, which is perhaps the most widely utilized in the finite element literature, is the one based on the multiplicative splitting of the deformation gradient. In the succeeding text, we outline a different mixed variational principle that does not require any splitting of the deformation gradient whatsoever, and thus, it is free of any artifacts that such a splitting may introduce. In the remainder of the paper, this mixed variational principle is referred to as the **F**-formulation.

The basic idea is to introduce a function \hat{W} such that $W(\mathbf{X}, \mathbf{F}) = \hat{W}(\mathbf{X}, \mathbf{F}, J)$, when $J = \det \mathbf{F}$ together with its partial Legendre transformation

$$\hat{W}^*(\mathbf{X}, \mathbf{F}, \hat{q}) = \max_J \left\{ \hat{q}(J - 1) - \hat{W}(\mathbf{X}, \mathbf{F}, J) \right\}. \quad (7)$$

Provided that \hat{W} is convex in its argument J , the following duality relation holds:

$$\hat{W}(\mathbf{X}, \mathbf{F}, J) = \max_{\hat{q}} \left\{ \hat{q}(J - 1) - \hat{W}^*(\mathbf{X}, \mathbf{F}, \hat{q}) \right\}. \quad (8)$$

Direct substitution of relation (8) in the classical principle of minimum potential energy (2)–(3) renders the following alternative mixed variational principle:

$$\hat{\Pi}(\mathbf{u}, \hat{p}) = \min_{\mathbf{v} \in \mathcal{K}} \max_{\hat{q} \in \mathcal{Q}} \hat{\Pi}(\mathbf{v}, \hat{q}), \quad (9)$$

with

$$\hat{\Pi}(\mathbf{v}, \hat{q}) = \int_{\Omega} \left\{ -\hat{W}^*(\mathbf{X}, \mathbf{F}(\mathbf{v}), \hat{q}) + \hat{q}[\det \mathbf{F}(\mathbf{v}) - 1] \right\} d\mathbf{X} - \int_{\Omega} \mathbf{f} \cdot \mathbf{v} d\mathbf{X} - \int_{\Gamma_t} \mathbf{t}^0 \cdot \mathbf{v} dS. \quad (10)$$

In the aforementioned expression, \mathcal{Q} denotes the set of square-integrable scalar functions, and the maximizing scalar field \hat{p} is directly related to the equilibrium Cauchy hydrostatic pressure field $p \doteq \text{tr} \boldsymbol{\sigma}$ via

$$p = \hat{p} - \frac{1}{3 \det \mathbf{F}} \frac{\partial \hat{W}^*}{\partial \mathbf{F}}(\mathbf{X}, \mathbf{F}, \hat{p}) : \mathbf{F}, \quad (11)$$

where we recall that the Cauchy stress tensor $\boldsymbol{\sigma}$ is given in terms of the first Piola–Kirchhoff stress tensor \mathbf{P} by the relation $\boldsymbol{\sigma} = J^{-1} \mathbf{P} \mathbf{F}^T$.

The weak form of the Euler–Lagrange equations associated with the variational principle (9)–(10) reads as

$$\begin{aligned} D \hat{\Pi}(\mathbf{u}, \hat{p}) \cdot \mathbf{v} &= \int_{\Omega} \left[-\frac{\partial \hat{W}^*}{\partial \mathbf{F}}(\mathbf{X}, \mathbf{F}(\mathbf{u}), \hat{p}) + \hat{p} \frac{\partial}{\partial \mathbf{F}}(\det \mathbf{F}(\mathbf{u})) \right] : \nabla \mathbf{v} d\mathbf{X} \\ &\quad - \int_{\Omega} \mathbf{f} \cdot \mathbf{v} d\mathbf{X} - \int_{\Gamma_t} \mathbf{t}^0 \cdot \mathbf{v} dS = 0 \quad \forall \mathbf{v} \in \mathcal{K}^0, \end{aligned} \quad (12)$$

$$D \hat{\Pi}(\mathbf{u}, \hat{p}) \cdot \hat{q} = \int_{\Omega} \left[\det \mathbf{F}(\mathbf{u}) - 1 - \frac{\partial \hat{W}^*}{\partial \hat{p}}(\mathbf{X}, \mathbf{F}(\mathbf{u}), \hat{p}) \right] \hat{q} d\mathbf{X} = 0 \quad \forall \hat{q} \in \mathcal{Q}. \quad (13)$$

When linearized, Equations (12) and (13) take the form

$$D \hat{\Pi}(\mathbf{u}, \hat{p}) \cdot \mathbf{v} + a_{\mathbf{u}, \hat{p}}(\mathbf{v}, \mathbf{w}) + b_{\mathbf{u}}(\mathbf{v}, \hat{g}) = 0 \quad \forall \mathbf{v} \in \mathcal{K}^0, \quad (14)$$

$$D \hat{\Pi}(\mathbf{u}, \hat{p}) \cdot \hat{q} + b_{\mathbf{u}}(\mathbf{w}, \hat{q}) + c_{\mathbf{u}, \hat{p}}(\hat{q}, \hat{g}) = 0 \quad \forall \hat{q} \in \mathcal{Q}, \quad (15)$$

with

$$a_{\mathbf{u}, \hat{p}}(\mathbf{v}, \mathbf{w}) = \int_{\Omega} \nabla \mathbf{v} : \left[-\frac{\partial^2 \hat{W}^*}{\partial \mathbf{F}^2}(\mathbf{X}, \mathbf{F}(\mathbf{u}), \hat{p}) + \hat{p} \frac{\partial^2}{\partial \mathbf{F}^2}(\det \mathbf{F}(\mathbf{u})) \right] : \nabla \mathbf{w} d\mathbf{X}, \quad (16)$$

$$b_{\mathbf{u}}(\mathbf{v}, \hat{g}) = \int_{\Omega} \nabla \mathbf{v} : \frac{\partial}{\partial \mathbf{F}}(\det \mathbf{F}(\mathbf{u})) \hat{g} d\mathbf{X}, \quad (17)$$

$$c_{\mathbf{u}, \hat{p}}(\hat{q}, \hat{g}) = - \int_{\Omega} \hat{q} \frac{\partial^2 \hat{W}^*}{\partial \hat{p}^2}(\mathbf{X}, \mathbf{F}(\mathbf{u}), \hat{p}) \hat{g} d\mathbf{X}, \quad (18)$$

where \mathbf{w} and \hat{g} denote the increments in the displacement and the pressure-like fields.

2.3. The commonly used two-field mixed variational formulation

The commonly used two-field mixed variational principle in the finite element literature requires the multiplicative splitting of the deformation gradient into a deviatoric part, $\bar{\mathbf{F}}$, and a hydrostatic part, $(\det \mathbf{F})^{\frac{1}{3}} \mathbf{I}$, namely, $\mathbf{F} = (\det \mathbf{F})^{\frac{1}{3}} \bar{\mathbf{F}}$ [23, 28, 32, 33]. For this reason, we shall denote this mixed variational principle as the $\bar{\mathbf{F}}$ -formulation in the sequel. Together with the splitting, a function \bar{W} is introduced such that $W(\mathbf{X}, \mathbf{F}) = \bar{W}(\mathbf{X}, \bar{\mathbf{F}}, J)$, when $J = \det \mathbf{F}$. Again, it can be transformed to a new function \bar{W}^* through

$$\bar{W}^*(\mathbf{X}, \bar{\mathbf{F}}, q) = \max_J \{q(J-1) - \bar{W}(\mathbf{X}, \bar{\mathbf{F}}, J)\}, \quad (19)$$

and the duality relation

$$\bar{W}(\mathbf{X}, \bar{\mathbf{F}}, J) = \max_q \{q(J-1) - \bar{W}^*(\mathbf{X}, \bar{\mathbf{F}}, q)\} \quad (20)$$

holds if $\bar{W}(\mathbf{X}, \bar{\mathbf{F}}, J)$ is assumed to be convex in J .

By substitution of relation (20) in (2)–(3), the $\bar{\mathbf{F}}$ -formulation can be obtained as

$$\bar{\Pi}(\mathbf{u}, p) = \min_{\mathbf{v} \in \mathcal{K}} \max_{q \in \mathcal{Q}} \bar{\Pi}(\mathbf{v}, q), \quad (21)$$

with

$$\bar{\Pi}(\mathbf{v}, q) = \int_{\Omega} \left\{ -\bar{W}^*(\mathbf{X}, \bar{\mathbf{F}}(\mathbf{v}), q) + q[\det \mathbf{F}(\mathbf{v}) - 1] \right\} d\mathbf{X} - \int_{\Omega} \mathbf{f} \cdot \mathbf{v} d\mathbf{X} - \int_{\Gamma_t} \mathbf{t}^0 \cdot \mathbf{v} dS. \quad (22)$$

Here, the maximizing scalar field p is identified exactly as the equilibrium Cauchy hydrostatic pressure field $p = \text{tr} \boldsymbol{\sigma}$.

The weak forms of the Euler–Lagrange equations associated with the aforementioned $\bar{\mathbf{F}}$ -formulation and their linearized forms can be obtained in a similar manner as the ones of the \mathbf{F} -formulation that are presented in the preceding subsection.

3. POLYGONAL FINITE ELEMENTS

In this section, finite element approximations on polygonal meshes are discussed. First, we present the construction of the displacement and pressure spaces for polygonal finite elements. This leads to the subsequent finite element approximations of the weak forms for the displacement-based and mixed variational formulations. Finally, numerical quadrature schemes for polygonal finite elements are compared and discussed.

3.1. Displacement and pressure spaces on polygonal discretizations

While mesh topology has an influence on the performance of the FEM, the choice of finite element spaces (e.g., interpolants) is also important. Consider \mathcal{T}_h to be a partition of the domain Ω into non-overlapping polygons. The displacement space is chosen to be a conforming finite dimensional space denoted \mathcal{K}_h with the degrees of freedom being the displacements at each vertex of the mesh. At the element level, the displacement field is approximated by a linear combination of a set of barycentric coordinates. If we denote $\mathcal{V}(E)$ as the space that spans barycentric coordinates φ_i over polygon E with n vertices, that is, $\mathcal{V}(E) = \text{span} \{ \varphi_1, \dots, \varphi_n \}$, the finite dimensional space \mathcal{K}_h is defined as

$$\mathcal{K}_h = \{ \mathbf{v}_h \in [C^0(\Omega)]^2 \cap \mathcal{K} : \mathbf{v}_h|_E \in [\mathcal{V}(E)]^2, \forall E \in \mathcal{T}_h \}. \tag{23}$$

In the literature, there are quite a few barycentric coordinates available to construct finite dimensional spaces on planar polygons [34–41]. By definition, they all satisfy the Kronecker-delta property, that is, $\varphi_i(\mathbf{X}_j) = \delta_{ij}$. Moreover, all the barycentric coordinates vary linearly along the edges, and in the interior, they are positive. Finally, all barycentric coordinates interpolate linear fields exactly, which means

$$\sum_{i=1}^n \varphi_i(\mathbf{X}) = 1, \quad \sum_{i=1}^n \varphi_i(\mathbf{X}) \mathbf{X}_i = \mathbf{X}, \tag{24}$$

where \mathbf{X}_i is the position vector of vertex i .

Most of the barycentric coordinates require the polygon to be convex, such as Wachspress coordinates, and barycentric coordinates constructed from iso-parametric mapping. To handle discretizations containing initially non-convex polygons, including those with collinear vertices, we adopt the Mean Value coordinates [42], which can be constructed on arbitrary polygons, as shown in Figures 1(b) and 1(c). The Mean Value coordinates are constructed directly on physical elements. In other words, no iso-parametric mapping is employed.

For an n -sided polygon E with i th vertex located at \mathbf{X}_i , its Mean Value coordinate for vertex i is defined as [42]:

$$\varphi_i(\mathbf{X}) = \frac{w_i(\mathbf{X})}{\sum_{j=1}^n w_j(\mathbf{X})}, \tag{25}$$

with w_i given by

$$w_i(\mathbf{X}) = \frac{\tan \left[\frac{\beta_{i-1}(\mathbf{X})}{2} \right] + \tan \left[\frac{\beta_i(\mathbf{X})}{2} \right]}{\| \mathbf{X} - \mathbf{X}_i \|}, \tag{26}$$

where the angle $\beta_i(\mathbf{X})$ is the angle defined in Figure 1(a).

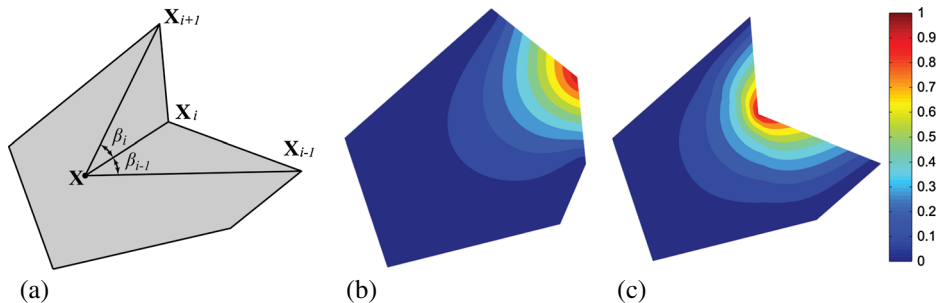


Figure 1. (a) Illustration of angles β_i used to define the interpolant w_i . (b) Contour plot of a Mean Value coordinate basis φ_i over a convex polygon. (c) Contour plot of a Mean Value coordinate basis φ_i over a non-convex polygon.

In two-field mixed FEMs, the approximation of the additional scalar field is also needed. As the most simple form of interpolation that leads to a stable approximation on polygonal meshes [10], a piecewise constant interpolation of the scalar field is adopted. It assumes the second field to be constant over each element. Accordingly, the basis functions used for this interpolation are

$$\chi_E(\mathbf{X}) = \begin{cases} 1, & \text{if } \mathbf{X} \in E \\ 0, & \text{otherwise} \end{cases} \quad \forall E \in \mathcal{T}_h. \tag{27}$$

Consider the pressure-like field \hat{p} as an example. As a consequence, the finite dimensional space for the pressure field consists of piecewise constant functions over Ω , denoted by \mathcal{Q}_h . It is a subspace of \mathcal{Q} and is defined as

$$\mathcal{Q}_h = \{\hat{q}_h \in \mathcal{Q} : \hat{q}_h|_E = \text{constant}, \forall E \in \mathcal{T}_h\}. \tag{28}$$

3.2. Conforming finite element approximations

Considering the finite element space for displacement $\mathcal{K}_h \subseteq \mathcal{K}$ for the mesh \mathcal{T}_h , the Galerkin approximation of the displacement-based formulation in Equation (4) consists of finding $\mathbf{u}_h \in \mathcal{K}_h$ such that

$$G(\mathbf{u}_h, \mathbf{v}_h) = 0 \quad \forall \mathbf{v}_h \in \mathcal{K}_h^0, \tag{29}$$

where \mathcal{K}_h^0 is defined as $\mathcal{K}_h^0 = \mathcal{K}_h \cap \mathcal{K}^0$.

Additionally, by introducing the finite element space for the pressure field, $\mathcal{Q}_h \subseteq \mathcal{Q}$, the Galerkin approximation of the two-field variational principle can also be obtained. Take the **F**-formulation for example, its Galerkin approximation consists of finding $(\mathbf{u}_h, \hat{p}_h) \in \mathcal{K}_h \times \mathcal{Q}_h$ such that

$$D\hat{\Pi}(\mathbf{u}_h, \hat{p}_h) \cdot \mathbf{v}_h = 0 \quad \forall \mathbf{v}_h \in \mathcal{K}_h^0, \tag{30}$$

$$D\hat{\Pi}(\mathbf{u}_h, \hat{p}_h) \cdot \hat{q}_h = 0 \quad \forall \hat{q}_h \in \mathcal{Q}_h. \tag{31}$$

For a given discretization, the quantities in the aforementioned nonlinear equations and their linearizations are typically obtained by assembling the contributions from the element levels. In this paper, we adopt standard procedures, which can be found in FEM textbooks, for example, [22, 24].

3.3. Quadrature scheme

Unlike triangles and quads, there is no standard quadrature rule available for general irregular polygons with n sides ($n \geq 5$). Alternatively, triangulation or quadrangulation schemes are usually used in the literature, which subdivide each polygon into triangles or quadrilaterals and applies the standard Gauss quadrature rules in each region [7, 10]. An illustration of these schemes is shown in Figure 2. The triangulation scheme is more flexible, as it can handle certain non-convex polygons where the quadrangulation schemes may lose validity. An example is shown in Figure 2(c) and 2(d)

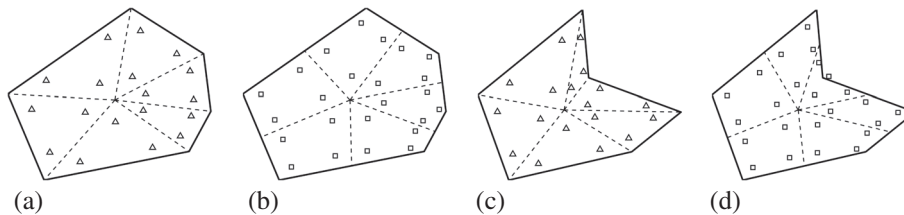


Figure 2. Illustration of the ‘triangulation’ and ‘quadrangulation’ schemes for general polygons in physical domain: (a) triangulation scheme for a convex polygon; (b) quadrangulation scheme for a convex polygon; (c) triangulation scheme for a non-convex polygon; and (d) quadrangulation scheme for a non-convex polygon (a quadrature point is outside of the polygon.)

where the quadrangulation scheme gives one quadrature point outside the polygon while the triangulation scheme does not. Because Mean Value coordinates are adopted with the purpose to handle non-convex elements and elements with collinear vertices, the triangulation scheme is used in this paper. For three-sided and four-sided polygons, the standard Gauss quadrature rules are used instead. It is worthwhile noting that, because the finite element spaces for polygonal elements include non-polynomial (e.g., rational) functions, the quadrature schemes that are discussed earlier can lead to consistency errors that do not vanish with mesh refinement [43]. As a result, the nonlinear version of the patch test, which provides a measure of the polynomial consistency, is not passed, even in the asymptotic sense, on polygonal meshes. This leads to a deterioration of the convergence of the finite element solutions. As will be shown in our numerical studies in Section 4, when the mesh size h becomes sufficiently small, the consistency errors start to dominate and the convergence rates of the error norms can exhibit noticeable decreases [43]. However, we note that, for the range of the mesh sizes considered in this paper, the consistency errors are still dominated by the discretization errors in finite element approximations, and therefore, the triangular scheme adopted in this paper is sufficiently accurate.

4. NUMERICAL ASSESSMENT

In this section, two numerical examples are presented with the aim of investigating the convergence, accuracy, and stability of the polygonal finite elements. The first example considers the problem of a cylindrical shell expanding under hydrostatic loading, a non-trivial problem for which there is a closed-form solution available. The second example considers the standard Cook's membrane problem to demonstrate the accuracy and numerical stability of the polygonal elements [44].

Throughout this section, conditions of plane strain are assumed, and the material is considered to be a neo-Hookean solid characterized by the stored-energy function

$$W(\mathbf{X}, \mathbf{F}) = \frac{\mu}{2} [\mathbf{F} : \mathbf{F} - 3] - \mu (\det \mathbf{F} - 1) + \frac{3\kappa + \mu}{6} (\det \mathbf{F} - 1)^2, \quad (32)$$

where the material parameters μ and κ stand for the shear and bulk moduli of the solid in its ground state. By choosing $\kappa = \infty$, expression (32) reduces to the standard incompressible neo-Hookean stored-energy function

$$W(\mathbf{X}, \mathbf{F}) = \begin{cases} \frac{\mu}{2} [\mathbf{F} : \mathbf{F} - 3] & \text{if } \det \mathbf{F} = 1 \\ +\infty & \text{otherwise} \end{cases}. \quad (33)$$

Upon recognizing that $\hat{W}(\mathbf{X}, \mathbf{F}, J) = \mu/2[\mathbf{F} : \mathbf{F} - 3] - \mu(J - 1) + (3\kappa + \mu)/6(J - 1)^2$, it is straightforward to deduce that the Legendre transformation (7) needed in the \mathbf{F} -formulation (9)–(10) is given by

$$\hat{W}^*(\mathbf{X}, \mathbf{F}, \hat{q}) = -\frac{\mu}{2} [\mathbf{F} : \mathbf{F} - 3] + \frac{3(\mu + \hat{q})^2}{2(3\kappa + \mu)} \quad (34)$$

in this case. For completeness and comparison purposes, we also present results for the commonly adopted $\bar{\mathbf{F}}$ -formulation.

The standard Newton–Raphson algorithm is employed to solve the nonlinear system of equations, and each loading step is regarded as convergent once the norm of the residual reduces below 10^{-10} times that of the initial residual.

4.1. Inflation of a cylindrical shell

The inflation problem of a cylindrical shell is considered in this subsection to verify the convergence of the mixed polygonal finite element approximation. As illustrated in Figure 3(a), the shell is taken

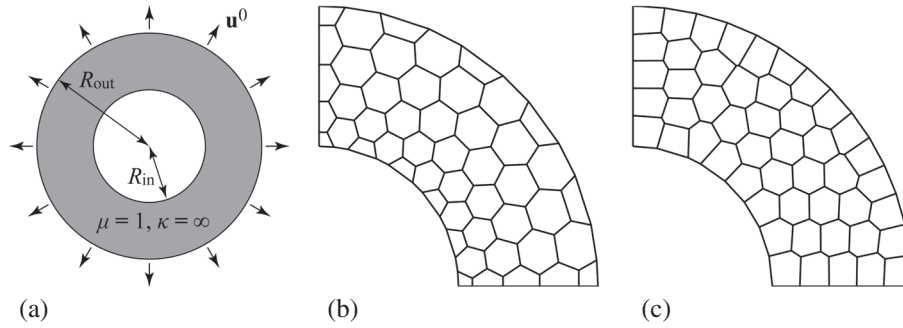


Figure 3. (a) Domain description for the problem. (b) A structured hexagonal-dominant mesh with 50 elements. (c) A centroidal Voronoi tessellation mesh with 50 elements.

to have inner radius R_{in} and outer radius R_{out} in its undeformed configuration. While its inner boundary is traction free, its outer boundary is subjected to the affine displacement

$$\mathbf{u}^0(\mathbf{X}) = (\lambda - 1)\mathbf{X}, \tag{35}$$

where λ is a prescribed loading parameter taking the value $\lambda = 1$ in the undeformed configuration; body forces are taken to be absent, that is, $\mathbf{f} = \mathbf{0}$. By restricting attention to neo-Hookean materials that are incompressible ($\kappa = \infty$) and deformations that are radially symmetric, the equilibrium Equations (12) and (13) can be solved exactly and in closed form to render:

$$\mathbf{u}(\mathbf{X}) = \left[\frac{r(R)}{R} - 1 \right] \mathbf{X}, \tag{36}$$

$$\nabla \mathbf{u}(\mathbf{X}) = \frac{1}{R^2} \left[r'(R) - \frac{r(R)}{R} \right] \mathbf{X} \otimes \mathbf{X} + \left[\frac{r(R)}{R} - 1 \right] \mathbf{I}, \tag{37}$$

$$p(\mathbf{X}) = -\frac{2\mu}{3} [r'(R)]^2 + \frac{\mu}{3} \left\{ \frac{[r(R)]^2}{R^2} + 1 \right\} + \frac{\mu (\lambda^2 - R_{out}^2) (R^2 - R_{in}^2)}{(\lambda^2 - R_{out}^2 + R^2) (\lambda^2 - R_{out}^2 + R_{in}^2)} + \mu \ln \frac{R r(R_{in})}{R_{in} r(R)}, \tag{38}$$

$$\hat{p}(\mathbf{X}) = p(\mathbf{X}) - \frac{\mu}{3} \left\{ [r'(R)]^2 + \frac{[r(R)]^2}{R^2} + 1 \right\}, \tag{39}$$

where

$$r(R) = \sqrt{R^2 + \lambda^2 - R_{out}^2}, \tag{40}$$

$R = |\mathbf{X}|$ and the notation $r' = dr/dR$ has been utilized for convenience.

Having the exact closed-form solutions (36)–(39) at our disposal, we now turn to evaluate the convergence of the polygonal finite element approximation within the context of the mixed variational formulation (9)–(10). In the finite element models, making use of symmetry, only a quadrant of the domain needs to be modeled. Two discretizations, centroidal Voronoi tessellation (CVT) mesh and structured hexagonal-dominant mesh, are considered. Figures 3(b) and 3(c) illustrate depictions of such discretizations.

Three measures of error are utilized to evaluate the convergence of the displacement field \mathbf{u} and hydrostatic pressure field p , including the normalized \mathcal{L}^2 -norms and \mathcal{H}^1 -seminorm, which are defined by the following expressions:

$$\epsilon_{0,\mathbf{u}} = \left[\frac{\int_{\Omega} (\mathbf{u} - \mathbf{u}_h) \cdot (\mathbf{u} - \mathbf{u}_h) d\mathbf{X}}{\int_{\Omega} \mathbf{u} \cdot \mathbf{u} d\mathbf{X}} \right]^{\frac{1}{2}}, \quad (41)$$

$$\epsilon_{1,\mathbf{u}} = \left[\frac{\int_{\Omega} (\nabla \mathbf{u} - \nabla \mathbf{u}_h) : (\nabla \mathbf{u} - \nabla \mathbf{u}_h) d\mathbf{X}}{\int_{\Omega} \nabla \mathbf{u} : \nabla \mathbf{u} d\mathbf{X}} \right]^{\frac{1}{2}}, \quad (42)$$

$$\epsilon_{0,p} = \left[\frac{\int_{\Omega} (p - p_h)^2 d\mathbf{X}}{\int_{\Omega} p^2 d\mathbf{X}} \right]^{\frac{1}{2}}. \quad (43)$$

Because the \mathbf{F} -formulation does not directly yield the hydrostatic pressure field, a post-processing step is used to obtain the hydrostatic pressure field when its error is to be evaluated. According to Equation (11), within an element E , the recovered hydrostatic pressure field $p_h|_E$ is given by

$$p_h|_E = \hat{p}_h|_E - \frac{1}{3 \det(\mathbf{F}(\mathbf{u}_h))_E} \frac{\partial \hat{W}^*}{\partial \mathbf{F}}(\mathbf{X}, \langle \mathbf{F}(\mathbf{u}_h) \rangle_E, \hat{p}_h|_E) : \langle \mathbf{F}(\mathbf{u}_h) \rangle_E, \forall E \in \mathcal{T}_h \quad (44)$$

where $\langle \cdot \rangle_E$ is an average operator over element E , defined as

$$\langle \cdot \rangle_E = \frac{1}{|E|} \int_E (\cdot) d\mathbf{X}, \quad (45)$$

in which $|E|$ denotes the area of element E .

The convergence results are shown in Figures 4(a)–4(c), where the error measures are plotted against the average element diameter (h) at the deformation state of $\lambda = 3$. For the CVT meshes, each data point is obtained by averaging values from a set of five meshes with the same number of elements. Both numerical results from the $\bar{\mathbf{F}}$ -formulation and the \mathbf{F} -formulation indicate optimal convergence rates in the respective error norms. In particular, they display second-order convergence in the \mathcal{L}^2 -norm of the error in displacement field and linear convergences in the \mathcal{H}^1 -seminorm of the error in displacement field and the \mathcal{L}^2 -norm of the error in hydrostatic pressure field. In fact, the \mathcal{L}^2 -norm of the error in hydrostatic pressure field and the \mathcal{H}^1 -seminorm of the error in displacement field for meshes using the $\bar{\mathbf{F}}$ -formulation appear to converge at a slightly faster rate than $\mathcal{O}(h)$ for this problem. In terms of accuracy, numerical results obtained by finite element analysis using the \mathbf{F} -formulation are found to be more accurate for this problem, as indicated by comparing the magnitudes of the three error measures in the figures.

Additionally, for the numerical results of the CVT meshes, we observe a noticeable degradation of the convergence rates in the \mathcal{H}^1 -seminorm of the displacement field errors, as the mesh is refined for both formulations. This is similar to the behavior observed in the linear analysis [43] and is due to the persistence of consistency errors in the quadrature scheme used, which is discussed in Section 3.3. Again, we remark that the degradation only begins to show up when the mesh size h is smaller than 0.01. In the range of practical interest, however, the quadrature scheme used is sufficient and optimal convergence is retained.

When undergoing large deformation, local material interpenetration, due to element flipping, tends to occur in finite element analysis when the \mathbf{F} -formulation is used, an interesting behavior that is not observed with the $\bar{\mathbf{F}}$ -formulation. Figure 5(a) depicts a hexagonal element and its flipping in the deformed state. Although this appears to be unphysical, the flipping behavior is found to be helpful in some problems, allowing the elements to undergo larger deformation when subjected to constraints. A representative example is the cavitation problem, which will be presented in Section 5.3. Qualitatively speaking, the flipping behavior happens to preserve the area of the element according to the area constraint when a very large deformation field is imposed. As illustrated in Figure 5(a), the flipping causes a portion of the deformed element to have negative area, denoted by A_-^E , which helps the other portion with positive area A_+^E deform more while fulfilling the incompressibility constraint, that is, $A_0^E = A_+^E + A_-^E$, where A_0^E is the undeformed area of the element.

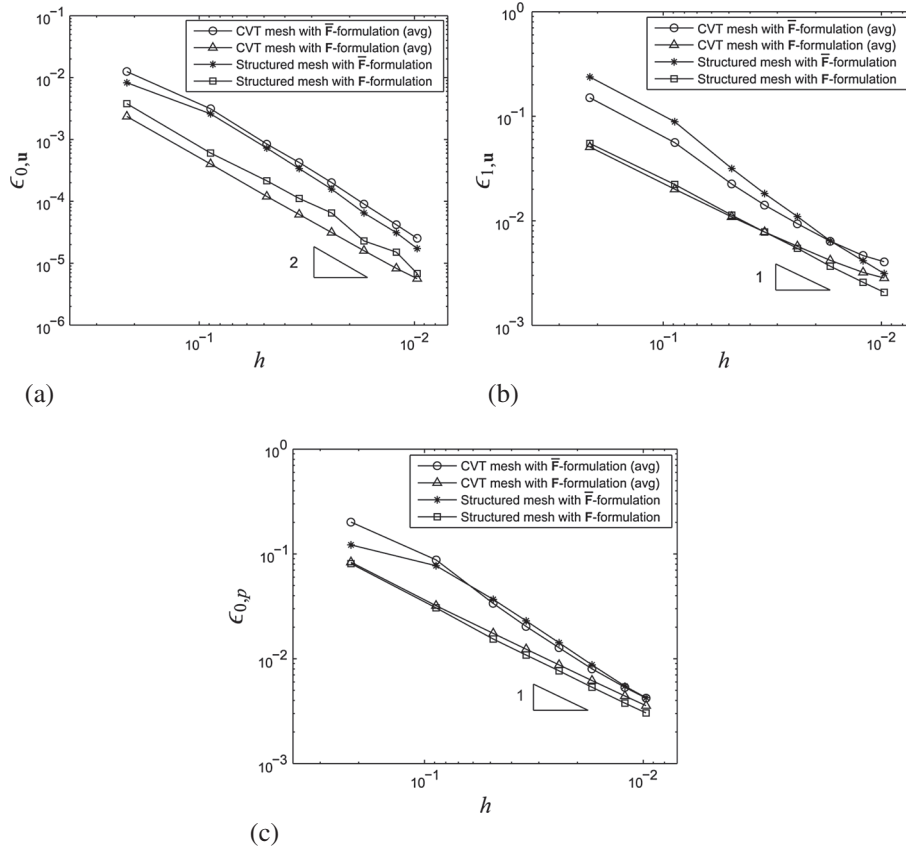


Figure 4. Plots of normalized error norms versus average mesh size h at the deformation state of $\lambda = 3$: (a) \mathcal{L}^2 -norm of the error in displacement field; (b) \mathcal{H}^1 -seminorm of the error in displacement field; and (c) \mathcal{L}^2 -norm of the error in hydrostatic pressure field.

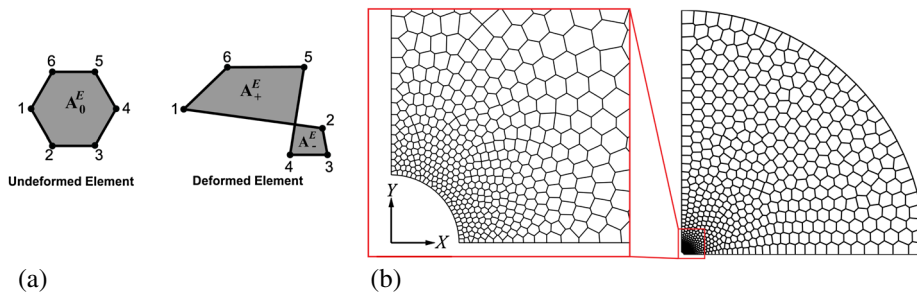


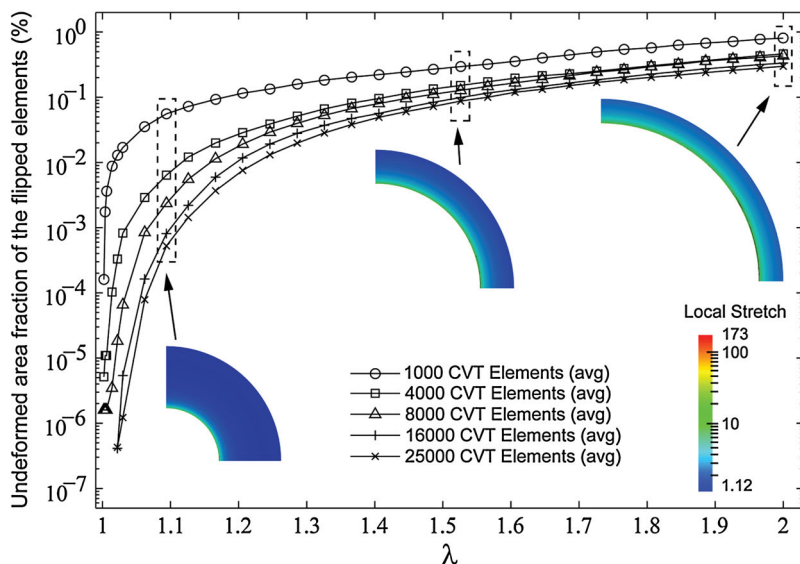
Figure 5. (a) A case where a hexagon flips in the deformed state. The area is preserved in this case, namely, $A_0^E = A_+^E + A_-^E$. (b) An example of a centroidal Voronoi tessellation mesh for the shell of $R_{in} = 0.01$ and $R_{out} = 1$.

To better understand the flipping behavior and its influence on the convergence of the mixed FEM, we perform a similar numerical study, which involves much larger local deformations that in turn introduce the flipping behavior. Consider a shell with a much smaller inner radius, $R_{in} = 0.01$, and the same outer radius $R_{out} = 1$, subjected to a hydrostatic displacement loading on the outer boundary until a global stretch of $\lambda = 2$ is reached. Only CVT meshes are considered in this example. Because the radius of the inner hole is much smaller than the radius of the outer boundary, the meshes are graded radially as shown in Figure 5(b). In the analysis, as the inner hole expands, the elements around it undergo very large deformations with stretches up to 150. Because of the large

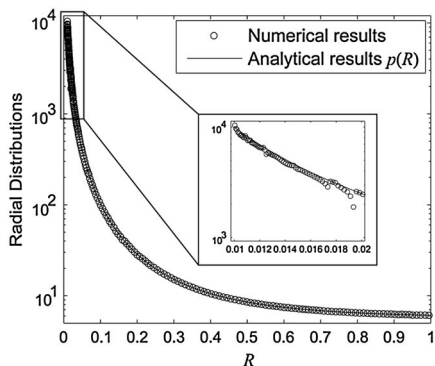
local deformations, we find that finite element approximations using the $\bar{\mathbf{F}}$ -formulation have difficulty in numerical convergence and hence are unable to capture the expansion of the inner hole, even with very refined meshes. In contrast, with the flipping behavior, the finite element models using the \mathbf{F} -formulation are capable of capturing the hole expansion. Table I summarizes the convergence of the normalized error norms for various refinements of the mesh. In this example, we include all the error measures, that is, the \mathcal{L}^2 -norm of the errors in the displacement field \mathbf{u} , the pressure-like field

Table I. Summary of the error norms as mesh refinement.

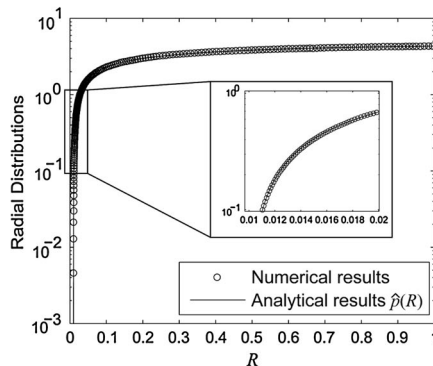
# element	h_{\min} (avg)	h_{\max} (avg)	$\epsilon_{0,\mathbf{u}}$ (avg)	$\epsilon_{1,\mathbf{u}}$ (avg)	$\epsilon_{0,p}$ (avg)	$\epsilon_{0,\hat{p}}$ (avg)
1000	1.63E-04	5.30E-02	6.26E-04	2.75E-02	8.39E-01	6.25E-03
4000	3.14E-04	3.01E-02	1.93E-04	1.38E-02	4.22E-01	3.96E-03
8000	1.70E-04	2.18E-02	1.12E-04	1.11E-02	2.20E-01	3.20E-03
16,000	1.06E-04	1.49E-02	6.53E-05	8.80E-03	1.12E-01	2.76E-03
25,000	7.78E-05	1.18E-02	4.69E-05	7.76E-03	7.36E-02	2.48E-03



(a)



(b)



(c)

Figure 6. (a) Quantification of the total area fractions of the flipped elements in the undeformed configuration. (b) Analytical solution and numerical result of the hydrostatic pressure fields p as a function of R along the X axis. (c) Analytical solution and numerical result of the pressure-like fields \hat{p} as a function of R along the X axis.

\hat{p} and the hydrostatic pressure field p , and the \mathcal{H}^1 -seminorm of the error in the displacement field \mathbf{u} . In the table, each value represents the average result of five randomly generated CVT meshes. As the number of elements increases, each error norm decreases and its magnitude stays within a reasonable range, as shown in Figures 4(a)–4(c). Meanwhile, we also find that the flipped elements are localized in regions where the deformation is large, that is, the region around the inner hole for this problem. In Figure 6(a), we quantify the total area fraction of the flipped elements in the undeformed configuration as a function of the applied global stretch λ . The figure illustrates that the area fraction of the flipped elements in the undeformed configuration decreases as the total number of elements increases and, for all the meshes considered, such an area fraction is below 1%. In summary, this example shows that the element flipping is a localized behavior and the mixed finite element approximation is convergent. In addition, a distinct difference is observed between the magnitude of the \mathcal{L}^2 -norms of p and \hat{p} . As a further investigation, in Figures 6(b) and 6(c), we plot the analytical solution and numerical results of p and \hat{p} along the X axis defined in Figure 5(b). In particular, a fine CVT mesh of 25,000 elements is used, and the numerical results along the X axis are obtained from those elements in the mesh whose edges are on the axis. From the figures, the numerical results of both fields are in good agreement with the analytical solutions. However, as illustrated in the zoomed sections, due to the nearly singular behavior of p , the numerical solutions of the pressure-like field \hat{p} are more accurate than those of the hydrostatic pressure field p .

4.2. Cook's benchmark problem

In order to demonstrate the performance of polygonal finite elements in terms of accuracy and stability, a Cook's benchmark example is performed with both lower order displacement and mixed finite elements. The problem consists of a tapered swept panel with dimensions depicted in Figure 7(a). The left boundary of the panel is fixed, and its right boundary is subjected to a uniform shear loading $\mathbf{t}^0 = [0, \tau]^T$ with $\tau = 0.1$. For simplicity, we assume the shear load is independent of deformation, and hence, it can be converted into nodal forces at the beginning of the finite element analysis. In addition to the CVT meshes, results by triangular and quadrilateral meshes are included for comparison. An illustration of the three types of meshes is shown in Figures 7(b)–7(d). Mesh refinements are performed to study the accuracy of the numerical results. In the study, we consider both compressible ($\mu = 1, \kappa = 1$) and incompressible ($\mu = 1, \kappa = \infty$) materials, analyzed by displacement-based finite elements and mixed finite elements, respectively. Figure 8(a) shows the convergence of the vertical displacement at point A, obtained by displacement-based finite elements, and Figure 8(b) shows the results by mixed finite elements using both the \mathbf{F} -formulation and $\bar{\mathbf{F}}$ -formulation. Again, each data point for the CVT mesh represents an average of the results from a set of five meshes. The reference values (11.7644 and 8.519, respectively) are obtained by very fine meshes of quadratic quadrilateral elements. In both cases, CVT meshes exhibit the fastest convergence and yield the most accurate results with a similar number of elements.

In the refinement study, a non-convergent performance for vertical deflection at point A is observed for the triangular meshes when mixed triangular elements are used, which results from

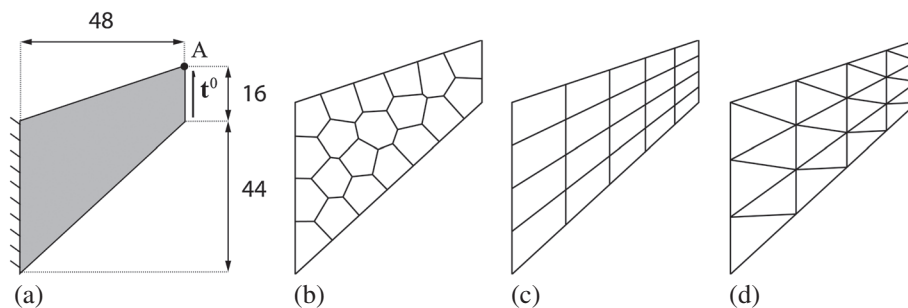


Figure 7. (a) Dimensions of the Cook membrane problem. (b) A centroidal Voronoi tessellation mesh consisting of 20 polygonal elements. (c) A quadrilateral mesh consisting of 20 linear elements. (d) A triangular mesh consisting of 24 linear elements.

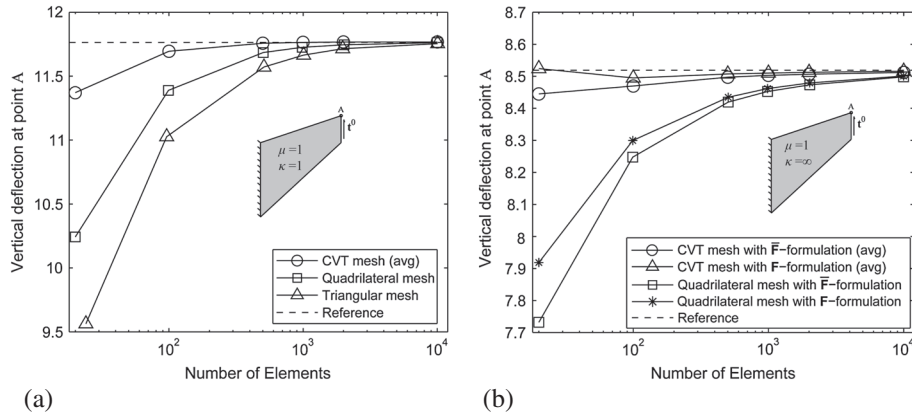


Figure 8. Convergence of the vertical deflection at point A for (a) displacement-based finite elements; and (b) mixed finite elements with constant pressure field.

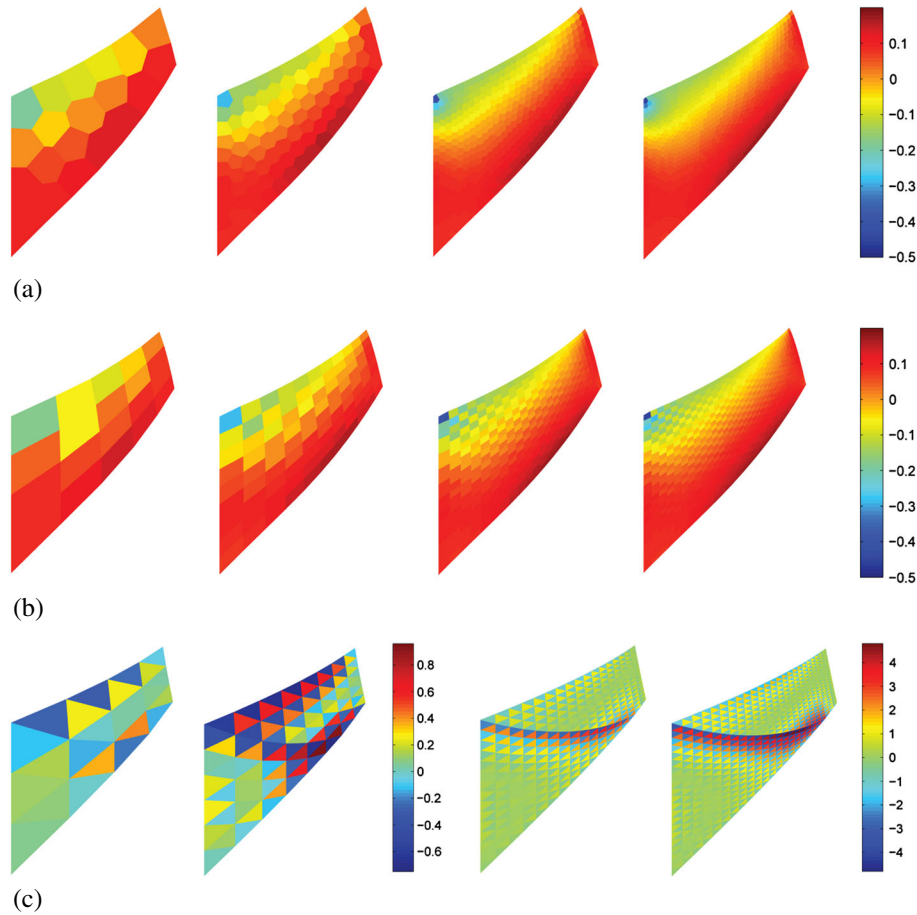


Figure 9. Fringe plots of hydrostatic pressure fields for (a) mixed polygonal elements; (b) mixed quadrilateral elements; and (c) mixed triangular elements.

their numerical instability and locking behavior due to the areal constraint. In order to qualitatively evaluate the numerical stability of the lower order mixed finite elements, fringe plots of the hydrostatic pressure fields from the \bar{F} -formulation in the final deformation state are shown in Figures 9(a)–9(c), for CVT meshes, quadrilateral meshes, and triangular meshes, respectively. From

the fringe plots, both results in triangular and quadrilateral meshes display numerical instabilities. They show either unphysical pressure fields or pressure fields containing spurious checkerboard modes. By contrast, results in CVT meshes exhibit smooth distributions of the pressure field, indicating the stability of the mixed polygonal elements. Identical performances are also observed for the fringe plots from the **F**-formulation.

5. APPLICATIONS

With the goal of illustrating the applications of polygonal finite elements to study nonlinear elastic materials undergoing finite deformations, this section presents three representative examples: (1) the finite deformation of an elastomer filled with an isotropic distribution of circular rigid particles; (2) the finite deformation of an elastomer filled with a periodic distribution of anisotropic rigid particles; and (3) cavitation instabilities in rubber. As demonstrated in the following subsections, polygonal elements provide geometric flexibility to model inclusions with arbitrary geometries and allow for the incorporation of periodic boundary conditions, as well as for bridging different length scales. In addition, the polygonal elements appear to be able to accommodate larger local distortions. In all the calculations that follow, conditions of plane strain are assumed.

5.1. Elastomers reinforced with circular filler particles

In this example, we study the nonlinear elastic response of a filled elastomer, comprised of a random distribution of monodisperse circular particles firmly bonded to the matrix material, subjected to uniaxial tension. The matrix is taken to be an incompressible Neo-Hookean rubber described by the stored-energy function (33) with $\mu = 1$. On the other hand, to model the rigid behavior of the particles, we consider them as incompressible Neo-Hookean solids with μ being five orders of magnitude larger than that of the matrix, namely, $\mu = 10^5$. Figure 10(a) shows the geometry of a representative volume element (RVE), which is repeated periodically, containing a total of 30 particles at 30% area fraction. The RVE is a square of dimension one by one. To account for periodicity, periodic boundary conditions [45] are applied to the RVE such that

$$\begin{aligned} u_k(1, X_2) - u_k(0, X_2) &= \langle \mathbf{F} \rangle_{k1} - \delta_{k1} \\ u_k(X_1, 1) - u_k(X_2, 0) &= \langle \mathbf{F} \rangle_{k2} - \delta_{k2} \quad \forall k = 1, 2 \end{aligned} \tag{46}$$

where δ_{kl} stands for the Kronecker delta and $\langle \mathbf{F} \rangle$ denotes the macroscopic deformation gradient with $\langle \cdot \rangle$ being an area average operator, that is,

$$\langle \cdot \rangle = \frac{1}{|\Omega|} \int_{\Omega} (\cdot) d\mathbf{X}. \tag{47}$$

Specifically, the macroscopic deformation gradient is $\langle \mathbf{F} \rangle = \lambda \mathbf{e}_1 \otimes \mathbf{e}_1 + \lambda^{-1} \mathbf{e}_2 \otimes \mathbf{e}_2$ in this case, where λ denotes the applied macroscopic stretch. Moreover, u_k and X_k ($k = 1, 2$) are the components

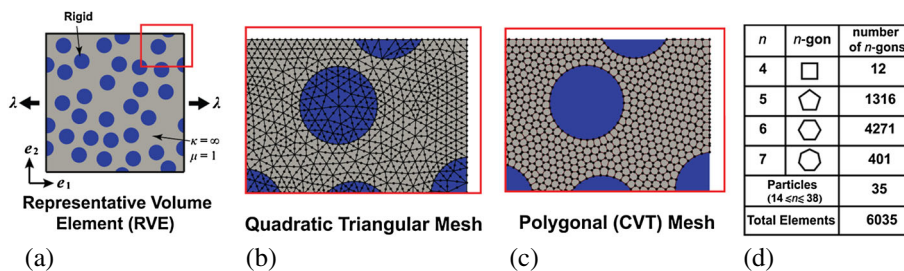


Figure 10. (a) Problem set-up and representative volume element. (b) Domain discretized by a standard triangular mesh composed of 7694 quadratic elements and 15,617 nodes total, with 12,112 nodes in the matrix phase. (c) Domain discretized by a polygonal mesh with 6035 n-gons and 12,232 nodes. (d) The composition of the polygonal mesh.

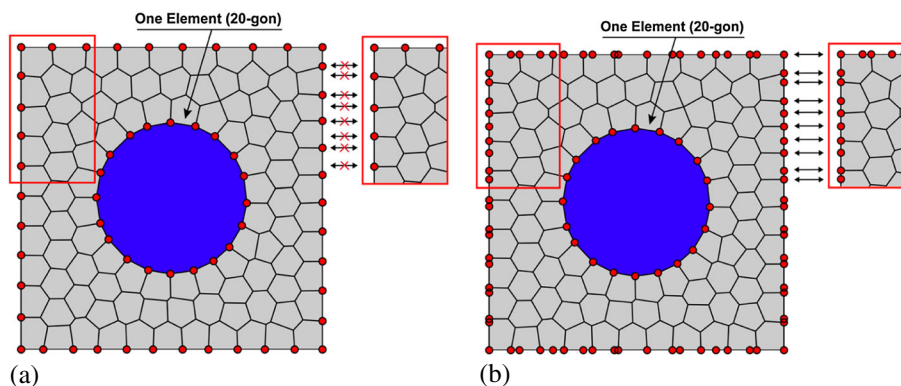


Figure 11. (a) Polygonal mesh with 100 elements, in which the circular inclusion is viewed as one element (20-gon). However, the mesh is NOT periodic on the boundary. (b) The periodic mesh is conveniently obtained by inserting nodes on the boundary without changing the overall mesh layout.

of the displacement field and the position vector in the undeformed configuration, respectively, referring to a Cartesian frame of reference with the origin placed at the left lower corner of the RVE, as shown in Figure 10(a). In order to apply periodic boundary conditions, periodic meshes with matching nodal distribution on the opposing edges of the RVE are required. For polygonal elements, because of their flexible geometry, the mesh can be locally modified to become periodic by simply inserting nodes at appropriate locations. In addition, the inclusions, irrespectively of their shape, can be modeled as single polygons. These concepts are illustrated in Figure 11.

Two discretizations are considered in this example: a polygonal mesh and, for comparison purposes, a triangular mesh. Figure 10(c) shows the polygonal mesh utilized to solve the problem where each particle is modeled by a single element, while Figure 10(b) depicts the triangular mesh. More specifically, the polygonal mesh consists of mixed linear elements with constant pressure. The triangular mesh, on the other hand, consists of hybrid quadratic elements with linear pressure (CPE6MH in ABAQUS) having a similar total number of DOFs, in the matrix phase, as the polygonal one.

The standard $\bar{\mathbf{F}}$ -formulation is adopted for the polygonal discretization and compared with results for the triangular mesh solved by ABAQUS. The deformed configurations of the RVE with polygonal elements and triangular elements are shown in Figures 12(a) and 12(b), at $\lambda = 2.1$ and $\lambda = 1.46$, respectively, which represent the maximum global deformations reached in each case. On the deformed meshes, the maximum stretch of each element is plotted, with those having maximum stretch of 5 or larger are shown in red. From the fringe plots of the elemental stretch field, it is clear that a greater number of polygonal elements undergo stretches greater than 5. In addition, the macroscopic quantities including the stored-energy function $\langle W \rangle$ and first Piola–Kirchhoff stress $\langle \mathbf{P} \rangle_{11}$ are plotted against the macroscopic stretch λ for the two meshes depicted in Figures 13(a) and 13(b). Both meshes agree reasonably well with the analytical solutions available in the literature for solids reinforced by a random and isotropic distribution of rigid particles [46]. At large strains, both finite element solutions display slightly stiffer responses.

5.2. Elastomers reinforced with anisotropic filler particles

At finite deformations, large local deformations within filled elastomers may be generated because of rigid particles coming into close proximity as discussed in the preceding example but may also be due to the large rigid rotations that anisotropic particles may undergo. In this example, we consider the latter case. To this end, we study the nonlinear elastic response of a filled elastomer, comprised of a periodic square distribution of elliptical particles firmly bonded to the matrix material, that is subjected to simple shear, that is, $\langle \mathbf{F} \rangle = \mathbf{I} + \gamma \mathbf{e}_1 \otimes \mathbf{e}_2$. As in the foregoing example, both the matrix and particles are considered to be Neo-Hookean solids. In order to directly compare the results with ABAQUS, the Neo-Hookean stored-energy function of the form

$$W(\mathbf{X}, \mathbf{F}) = \frac{\mu}{2} [\bar{\mathbf{F}} : \bar{\mathbf{F}} - 3] + \frac{\kappa}{2} (\det \mathbf{F} - 1)^2 \quad (48)$$

adopted in ABAQUS is used in this example. The shear and bulk moduli of the matrix are taken to be $\mu = 1$ and $\kappa = 100$, while those of the rigid particles are set to be $\mu = \kappa = 10^5$. Figure 14(a) shows the geometry of the RVE for the case of a particle of aspect ratio 4 and approximate area fraction 15%. The standard displacement formulation is utilized in this example, and we make use of a fine polygonal mesh, shown in Figure 14(c), with a rigid elliptical particle consisting of a single element (153-gon). Again, nodes are inserted on each boundary to guarantee a periodic mesh. For

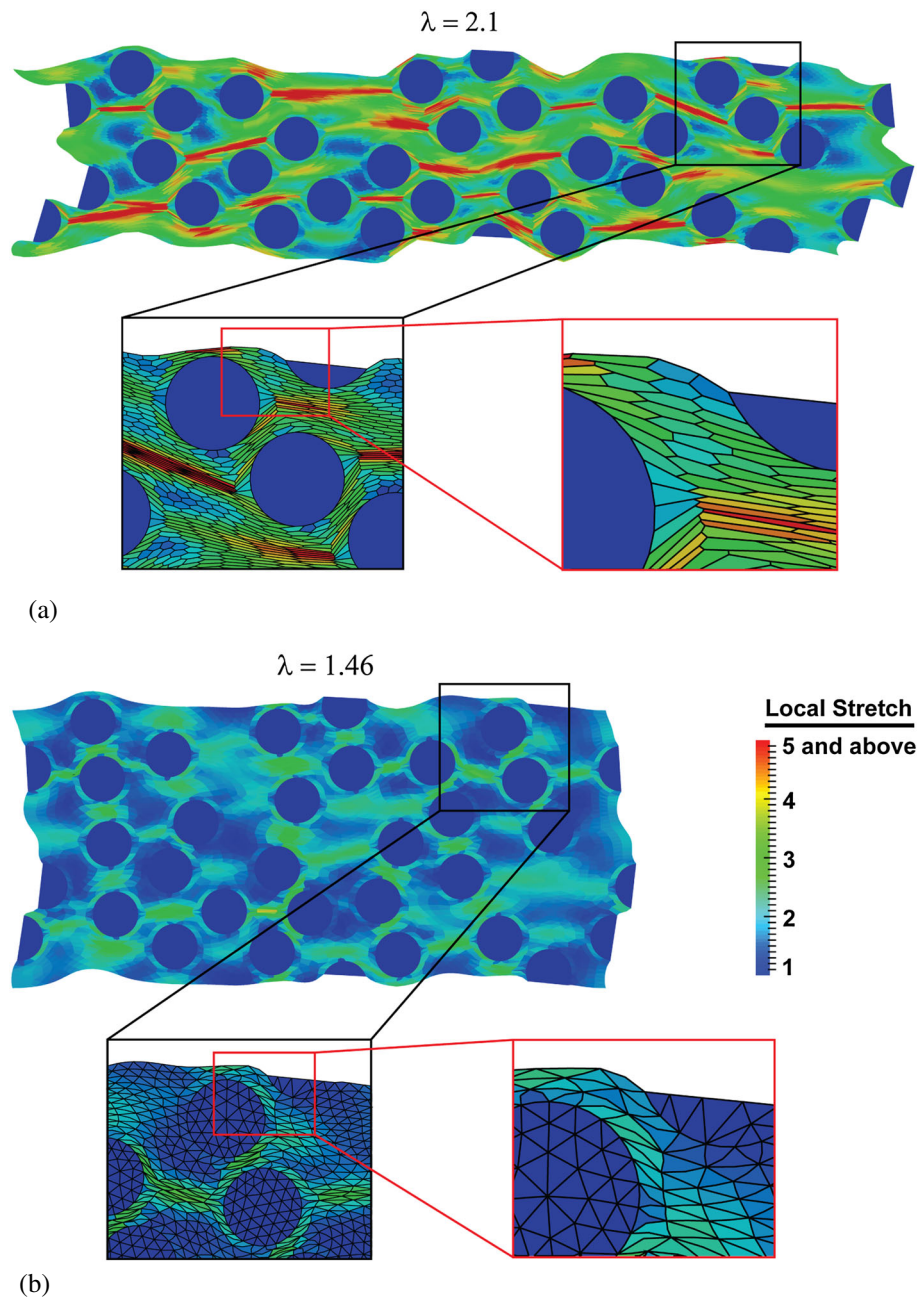


Figure 12. (a) Deformed shape using the polygonal mesh, in which the analysis stops at global stretch of $\lambda = 2.1$. (b) Deformed shape using the modified quadratic hybrid elements (CPE6MH) in ABAQUS, in which the analysis stops at $\lambda = 1.46$.

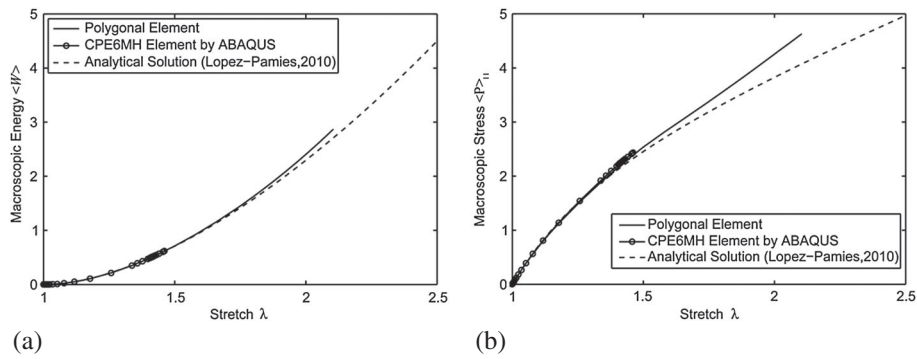


Figure 13. (a) Macroscopic stress $\langle \mathbf{P} \rangle_{11}$ versus the applied stretch λ . (b) Macroscopic stored-energy function $\langle W \rangle$ versus the applied stretch λ .

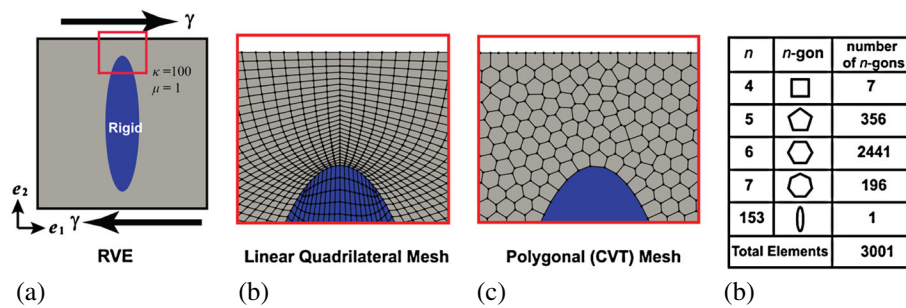


Figure 14. (a) Problem set-up and representative volume element. (b) Domain discretized by a quadrilateral mesh composed of 7100 elements and 7245 nodes total, with 5858 nodes in the matrix phase. (c) Domain discretized by a polygonal mesh having 3001 n -gons and 6164 nodes. (d) The composition of the polygonal mesh.

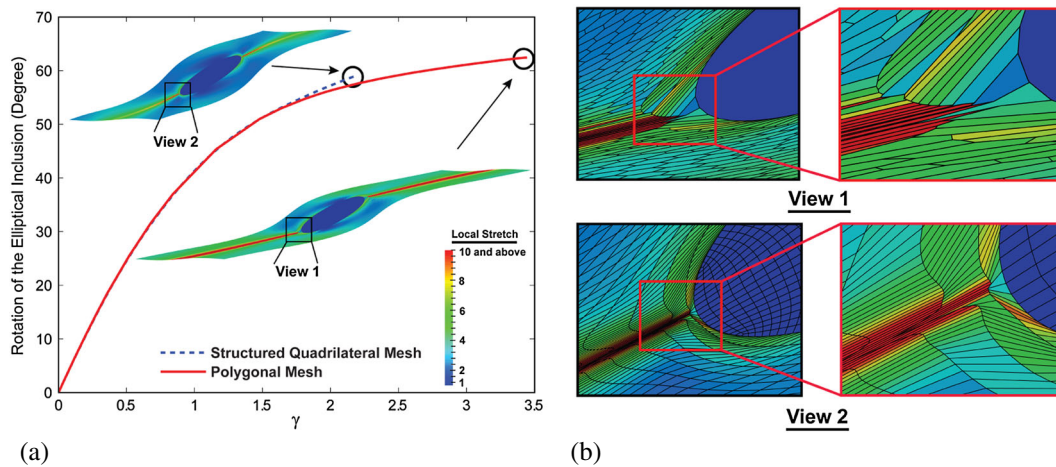


Figure 15. (a) Finite rotation of the rigid elliptical inclusion and final deformed representative volume element shape for both meshes. Analysis becomes non-convergent at $\gamma = 3.44$ for the polygonal mesh and at $\gamma = 2.18$ for the quadrilateral mesh. (b) Detailed views of the deformed polygonal and quadrilateral meshes.

comparison purposes, we also solve the problem with a structured mesh comprised of quadrilateral elements in ABAQUS. This conventional quadrilateral mesh is shown in Figure 14(b). Both meshes contain a similar number of DOFs in the matrix phase. Because of the applied shear deformation, the elliptical inclusion rotates. The angle of rotation as a function of the applied amount of shear γ is plotted in Figure 15(a). For further scrutiny of the result, the final deformed shapes of the RVE

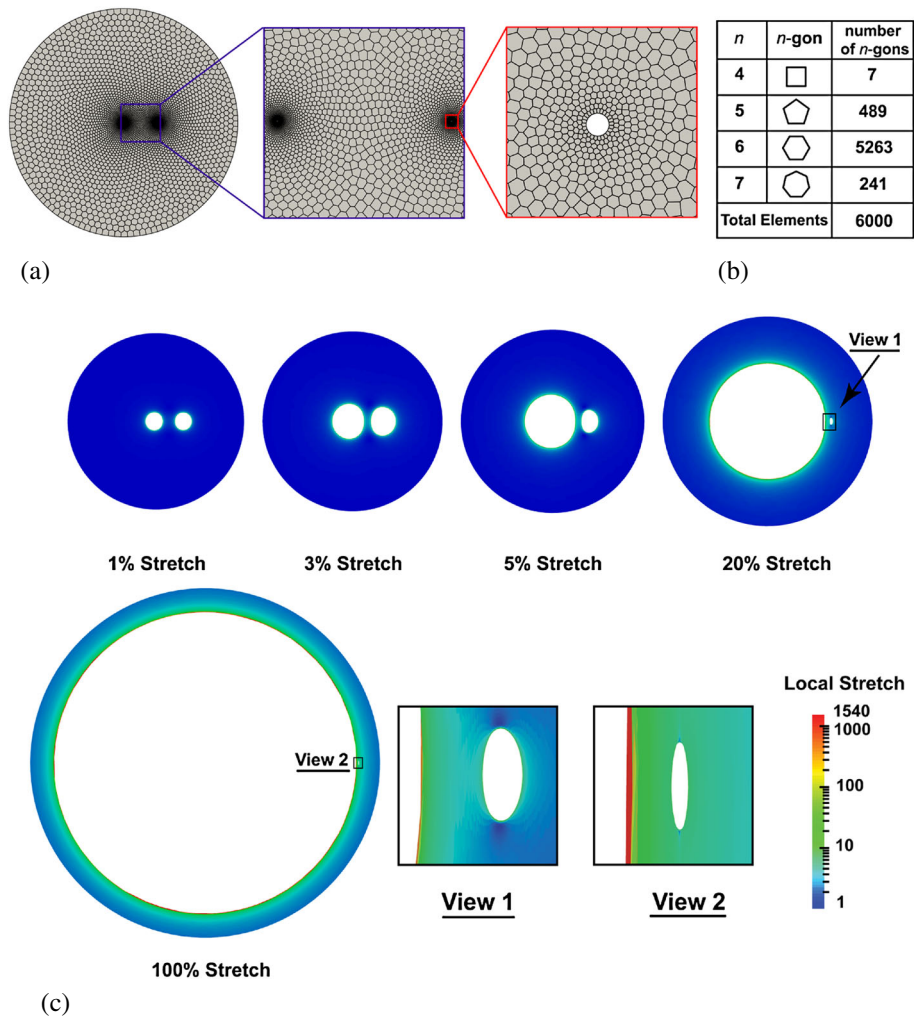


Figure 16. (a) The polygonal discretization of the disk domain of $R_d = 1$ centered at $(0, 0)$. Two circular defects with initial radius $R_c = 0.001$ are placed at $(0, 0)$ and $(0.3, 0)$. (b) The composition of the polygonal mesh. (c) The growth of the cavities modeled using a polygonal mesh under different levels of global stretches and detailed views.

and detailed views of the regions around the elliptical particle are displayed in Figures 15(a) and (b). The maximum stretches of each element are plotted on the deformed meshes, with those having maximum stretch of 10 or above shown in red. From the fringe plots, it is deduced that a greater number of polygonal elements undergo stretches greater than 10 when compared to the quadrilateral elements. Together with the preceding example of circular particles, this example demonstrates the ability of polygonal elements to handle large local deformations. The fact that the ‘particle’ consists of just a single element is also of great advantage to model limiting behaviors such as rigid or vacuous.

5.3. Cavitation in rubber

In this final example, we discuss cavitation in rubber, that is, the sudden ‘appearance’ of internal cavities in the interior of rubber at critically large loadings. Physically, this phenomenon corresponds to the growth of defects inherent in rubber [47]. Such defects can be of various natures (e.g., weak regions of the polymer network, actual holes, and particles of dust) and of various geometries ranging from submicron to supramicron in length scale [48]. Because of extreme local deformations in the

rubber surrounding the cavitating defects, the modeling of cavitation problems with standard finite elements is computationally challenging (see, e.g., [49, 50]).

As our first attempt to model such a problem, we study the cavitation problem employing the mixed polygonal finite elements. We consider a circular disk of radius $R_d = 1$ that contains two circular defects of radius $R_c = 0.001$ in its interior. The disk is centered at $(0, 0)$, and the two defects are placed at $(0, 0)$ and $(0.3, 0)$, respectively. The outer boundary of the disk is subjected to hydrostatic displacement loading until a radial stretch of 2 is reached. The constitutive properties of the disk are characterized by a one-term incompressible Lopez-Pamies material [51]:

$$W(\mathbf{X}, \mathbf{F}) = \begin{cases} \frac{3^{1-\alpha}}{2\alpha} \mu [(\mathbf{F} : \mathbf{F})^\alpha - 3^\alpha] & \text{if } \det \mathbf{F} = 1 \\ +\infty & \text{otherwise} \end{cases}, \quad (49)$$

with parameters $\mu = 1$ and $\alpha = 0.8$, which ensure appropriate growth conditions to allow for cavitation [52]. The corresponding complementary stored-energy function $\hat{W}^*(\mathbf{X}, \mathbf{F}, \hat{q})$ has the form

$$\hat{W}^*(\mathbf{X}, \mathbf{F}, \hat{q}) = -\frac{3^{1-\alpha}}{2\alpha} \mu [(\mathbf{F} : \mathbf{F})^\alpha - 3^\alpha]. \quad (50)$$

The discretization of such a problem is by no means an easy task as the mesh has to bridge two very different length scales: the scale of the defects (0.001) and the scale of the disk (1). Making use of the polygonal discretization, and exploiting the flexibility of Voronoi tessellations, we can easily obtain a mesh with two length scales by using specific density functions for mesh gradation [13] tailored to the problem at hand. Figure 16(a) illustrates the polygonal mesh of 6000 elements utilized in this example. Figure 16(c) shows snapshots of the disk at five different values of the applied hydrostatic stretch. Qualitatively, the growth of the two cavities is well captured. From the series of deformed configurations shown in Figure 16(c), both defects grow at the beginning of the loading. At around 5% stretch, the defect on the right stops growing and the one in the center starts to dominate and keeps growing until the final stretch 100% is reached. Extremely large local deformations take place within the elements surrounding the cavities. For those elements, flipping behavior is observed, a similar situation to that discussed in the numerical studies of Section 4.1. In contrast, finite element models with $\bar{\mathbf{F}}$ -formulation, which are typically employed in the finite element literature, do not contain flipped elements, yet the growth of the defects cannot be captured because of lack of numerical convergence. Again, we stress that the flipping behavior is helpful to capture the growth of the defects and will not affect the convergence and accuracy of the results in this problem.

6. CONCLUDING REMARKS

Finite element modeling of nonlinear elastic materials at finite deformations is a challenging task because of potentially large localized deformations. To address this issue, this work provides a framework to model such class of materials using polygonal finite elements. This framework is conducive to both displacement-based and general mixed variational formulations. In the later class of formulations, we derive both a formulation that does not require any splitting of the deformation gradient tensor (\mathbf{F} -formulation), and one that is based on the multiplicative splitting of the deformation gradient tensor ($\bar{\mathbf{F}}$ -formulation). At the element level, the mixed polygonal finite element consists of a linearly-complete displacement field approximated by a set of barycentric coordinates and a constant pressure field. These elements are shown to be numerically stable on Voronoi-type meshes without any additional stabilization treatment, and the convergence of the displacement field and pressure fields is verified in the range of mesh sizes of practical interest. Furthermore, applications involving filled elastomers and cavitation instabilities indicate that polygonal elements are well suited to model particulate microstructures (e.g., a single element may be used to model a rigid inclusion), incorporate periodic boundary conditions (leading to convenient discretization of RVEs), and bridge length scales (i.e., a tool for multiscale analysis). They also appear to be more tolerant of large local deformations than standard triangles and quads, while attaining accuracy and stability.

When subjected to large local deformation fields, an element flipping behavior in the deformed configuration is observed in the mixed finite element analysis using the \mathbf{F} -formulation. This effect is localized, and such behavior, as demonstrated by the present numerical studies, is found to be helpful in some problems where elements are allowed to deform further and still yield globally convergent solutions. However, a rigorous theoretical justification is needed for a better understanding of the flipping behavior and its influence on the quality of finite element solutions.

The available quadrature schemes on polygonal discretizations will lead to consistency errors that do not vanish under mesh refinement. The persistence of these errors can cause suboptimal convergence or even non-convergence in the finite element solutions, especially when nonlinear problems are involved. As a remedy, using sufficiently large number of quadrature points can lower the consistency errors such that they are dominated by the approximations errors. For linear polygonal elements, as shown from the numerical studies in this paper, the triangulation scheme with three quadrature points in each subdivided triangle appears to be sufficient to ensure accuracy and optimal convergence in practice. However, for higher-order or three-dimensional (3D) elements, the number of required integration points can become prohibitively large, which makes such approach less attractive from a practical point of view. Therefore, extension of the current framework to higher-order polygonal and 3D polyhedral elements requires better and more efficient quadrature schemes.

NOMENCLATURE

α	Material parameter for incompressible Lopez-Pamies material model reference to [51]
$\boldsymbol{\sigma}$	Cauchy stress tensor
$\chi_E(\mathbf{X})$	Basis function associated with polygon E for piecewise constant interpolation over the mesh \mathcal{T}_h
δ_{kl}	Kronecker delta
$\epsilon_{0,\mathbf{u}}, \epsilon_{1,\mathbf{u}}$	Normalized \mathcal{L}^2 -norm and \mathcal{H}^1 -seminorm of the error in finite element solution of displacement field \mathbf{u}
$\epsilon_{0,p}, \epsilon_{0,\hat{p}}$	Normalized \mathcal{L}^2 -norm of the errors in finite element solutions of the hydrostatic pressure field p and pressure-like field \hat{p}
$\Gamma_{\mathbf{t}}$	Part of the domain boundary $\partial\Omega$ where traction \mathbf{t}^0 is prescribed
$\Gamma_{\mathbf{u}}$	Part of the domain boundary $\partial\Omega$ where displacement \mathbf{u}^0 is prescribed
λ, γ	Applied macroscopic stretch and shear
$\langle \mathbf{F} \rangle$	Area average of deformation gradient \mathbf{F}
$\langle \mathbf{P} \rangle$	Area average of first Piola–Kirchhoff stress \mathbf{P}
$\langle W \rangle$	Area average of stored-energy function W
\mathcal{K}	Set of kinematically admissible displacement fields
\mathcal{K}^0	Set of kinematically admissible displacement fields that vanish on $\Gamma_{\mathbf{u}}$
\mathcal{K}_h	Finite dimensional displacement space defined over the mesh \mathcal{T}_h such that $\mathcal{K}_h \subseteq \mathcal{K}$
\mathcal{K}_h^0	Finite dimensional displacement space defined over the mesh \mathcal{T}_h such that $\mathcal{K}_h^0 = \mathcal{K}_h \cap \mathcal{K}^0$
\mathcal{Q}	Space consisting of square-integrable functions
\mathcal{Q}_h	Finite dimensional pressure space defined over mesh \mathcal{T}_h
\mathcal{T}_h	Partition of the domain into non-overlapping polygons
$\mathcal{V}(E)$	Space defined by linear combinations of a set of barycentric coordinates over polygon E
μ, κ	Shear and bulk moduli of elastic solids
∇	Gradient operator with respect to the undeformed configuration
Ω	Undeformed domain
$\hat{\Pi}(\mathbf{v}, \hat{q})$	Potential energy obtained from function $\hat{W}^*(\mathbf{X}, \mathbf{F}(\mathbf{v}), \hat{q})$
$\bar{\mathbf{F}}$	Deviatoric part of deformation gradient defined by $\bar{\mathbf{F}} = (\det \mathbf{F})^{-\frac{1}{3}} \mathbf{F}$

$\hat{W}(\mathbf{X}, \mathbf{F}, J)$	Function introduced such that $W(\mathbf{X}, \mathbf{F}) = \hat{W}(\mathbf{X}, \mathbf{F}, J)$ when $J = \det \mathbf{F}$
$\hat{W}^*(\mathbf{X}, \mathbf{F}, \hat{q})$	Function obtained by Legendre transformation of J in $\hat{W}(\mathbf{X}, \mathbf{F}, J)$
$\Pi(\mathbf{v})$	Potential energy obtained from stored-energy function $W(\mathbf{X}, \mathbf{F}(\mathbf{v}))$
\mathbf{F}	Deformation gradient tensor
\mathbf{f}	Body force per unit undeformed volume
\mathbf{P}	First Piola–Kirchhoff stress tensor
\mathbf{t}^0	Prescribed surface traction per unit undeformed area on Γ_t
\mathbf{u}	Unknown displacement field
\mathbf{u}^0	Prescribed displacement field on Γ_u
\mathbf{u}_h	Finite element solution of displacement field \mathbf{u}
\mathbf{v}	Trial displacement field
\mathbf{v}_h	Finite dimensional trial displacement field
\mathbf{w}	Incremental displacement field
\mathbf{X}	Initial position vector
φ_i	Mean Value coordinates associated with i th vertex of n -sided polygon E
$\bar{\Pi}(\mathbf{v}, q)$	Potential energy obtained from function $\bar{W}^*(\mathbf{X}, \bar{\mathbf{F}}(\mathbf{v}), q)$
\hat{g}	Incremental pressure-like field in the \mathbf{F} -formulation
\hat{p}	Unknown pressure-like field in the \mathbf{F} -formulation
$\bar{W}(\mathbf{X}, \bar{\mathbf{F}}, J)$	Function introduced such that $W(\mathbf{X}, \mathbf{F}) = \bar{W}(\mathbf{X}, \bar{\mathbf{F}}, J)$ when $J = \det \mathbf{F}$
$\bar{W}^*(\mathbf{X}, \bar{\mathbf{F}}, q)$	Function obtained by Legendre transformation of J in $\bar{W}(\mathbf{X}, \bar{\mathbf{F}}, J)$
h, h_{\max}, h_{\min}	Average, maximum, and minimum element diameters of the mesh \mathcal{T}_h
J	An independent scalar field introduced in $\hat{W}(\mathbf{X}, \mathbf{F}, J)$ and $\bar{W}(\mathbf{X}, \bar{\mathbf{F}}, J)$
p	Unknown hydrostatic pressure field
p_h, \hat{p}_h	Finite element solutions of hydrostatic pressure field p and pressure-like field \hat{p} , respectively
$p_h _E, \hat{p}_h _E$	Finite element solutions of hydrostatic pressure field p and pressure-like field \hat{p} over element E
q, \hat{q}	Trial hydrostatic pressure field and pressure-like field defined in the \mathbf{F} -formulation, respectively
q_h, \hat{q}_h	Finite dimensional trial hydrostatic pressure field and the pressure-like field used in the \mathbf{F} -formulation, respectively
$W(\mathbf{X}, \mathbf{F})$	Stored-energy as a function of deformation gradient \mathbf{F}
w_i, β_i	Weight function and angle associated with i th vertex of n -sided polygon E defined in mean value coordinates
$ \Omega $	Area of the undeformed domain Ω
$ E $	Area of undeformed polygon E

ACKNOWLEDGEMENTS

We acknowledge the support from the US National Science Foundation (NSF) through grant CMMI #1437535. The information presented in this paper is the sole opinion of the authors and does not necessarily reflect the views of the sponsoring agency.

REFERENCES

1. Ramier J. Comportement mécanique d'élastomères chargés, influence de l'adhésion chargeolymère, influence de la morphologie. *Ph.D. Thesis*, Institut National des Science Appliquées de Lyon, France, 2004.
2. Goudarzi T. Iterative and variational homogenization methods for particle-filled elastomers. *Ph.D. Thesis*, University of Illinois at Urbana-Champaign, USA, 2014.
3. Moraleda J, Segurado J, LLorca J. Finite deformation of incompressible fiber-reinforced elastomers: a computational micromechanics approach. *Journal of the Mechanics and Physics of Solids* 2009; **57**(9):1596–1613.
4. Wachspress EL. *A Rational Finite Element Basis*. Academic Press: New York, 1975.

5. Bishop JE. Simulating the pervasive fracture of materials and structures using randomly close packed Voronoi tessellations. *Computational Mechanics* 2009; **44**(4):455–471.
6. Gain AL, Talischi C, Paulino GH. On the virtual element method for three-dimensional elasticity problems on arbitrary polyhedral meshes. *eprint arXiv:1311.0932*, 11/2013.
7. Sukumar N, Tabarraei A. Conforming polygonal finite elements. *International Journal of Numerical Methods in Engineering* 2004; **61**(12):2045–2066.
8. Talischi C, Paulino GH, Pereira A, Menezes IFM. Polygonal finite elements for topology optimization: a unifying paradigm. *International Journal for Numerical Methods in Engineering* 2010; **82**:671–698.
9. Talischi C, Paulino GH, Pereira A, Menezes IFM. Polytop: a Matlab implementation of a general topology optimization framework using unstructured polygonal finite element meshes. *Structural and Multidisciplinary Optimization* 2012; **45**(3):329–357.
10. Talischi C, Pereira A, Paulino GH, Menezes IFM, Carvalho MS. Polygonal finite elements for incompressible fluid flow. *International Journal for Numerical Methods in Fluids* 2014; **74**:134–151.
11. Ebeida MS, Mitchell SA. Uniform random voronoi meshes. In *Proceedings of the 20th International Meshing Roundtable*. Springer: Berlin Heidelberg, 2012; 273–290.
12. Sieger D, Alliez P, Botsch M. Optimizing voronoi diagrams for polygonal finite element computations. In *Proceedings of the 19th international meshing roundtable*. Springer: Berlin Heidelberg, 2010; 335–350.
13. Talischi C, Paulino GH, Pereira A, Menezes IFM. Polymesher: a general-purpose mesh generator for polygonal elements written in Matlab. *Structural and Multidisciplinary Optimization* 2012; **45**(3):309–328.
14. Leon SE, Spring DW, Paulino GH. Reduction in mesh bias for dynamic fracture using adaptive splitting of polygonal finite elements. *International Journal for Numerical Methods in Engineering* 2014. DOI: 10.1002/nme.4744.
15. Spring DW, Leon SE, Paulino GH. Unstructured polygonal meshes with adaptive refinement for the numerical simulation of dynamic cohesive fracture. *International Journal of Fracture* 2014; **189**:33–57.
16. Boffi D, Brezzi F, Fortin M. *Mixed Finite Element Methods and Applications*. Springer: Berlin, 2013.
17. Oden JT, Kikuchi N. Finite element methods for constrained problems in elasticity. *International Journal for Numerical Methods in Engineering* 1982; **18**(5):701–725.
18. Chapelle D, Bathe KJ. The inf-sup test. *Computers & Structures* 1993; **47**(4):537–545.
19. Hughes TJR. *The Finite Element Method: Linear Static and Dynamic Finite Element Analysis*. Courier Dover Publications: Mineola, NY, 2012.
20. Biabanaki SOR, Khoei AR. A polygonal finite element method for modeling arbitrary interfaces in large deformation problems. *Computational Mechanics* 2012; **50**(1):19–33.
21. Biabanaki SOR, Khoei AR, Wriggers P. Polygonal finite element methods for contact-impact problems on non-conformal meshes. *Computer Methods in Applied Mechanics and Engineering* 2014; **269**:198–221.
22. Bonet J, Wood RD. *Nonlinear Continuum Mechanics for Finite Element Analysis*. Cambridge University Press: Cambridge, 2008.
23. Ogden RW. *Nonlinear Elastic Deformations*. Courier Dover Publications: Mineola, NY, 1997.
24. Wriggers P. *Nonlinear Finite Element Methods*, Vol. 4. Springer: Berlin, 2008.
25. Brink U, Stein E. On some mixed finite element methods for incompressible and nearly incompressible finite elasticity. *Computational Mechanics* 1996; **19**(1):105–119.
26. Chang TYP, Saleeb AF, Li G. Large strain analysis of rubber-like materials based on a perturbed lagrangian variational principle. *Computational mechanics* 1991; **8**(4):221–233.
27. Chen JS, Han W, Wu CT, Duan W. On the perturbed lagrangian formulation for nearly incompressible and incompressible hyperelasticity. *Computer Methods in Applied Mechanics and Engineering* 1997; **142**(3):335–351.
28. Simo JC, Taylor RL, Pister KS. Variational and projection methods for the volume constraint in finite deformation elasto-plasticity. *Computer Methods in Applied Mechanics and Engineering* 1985; **51**(1):177–208.
29. Sussman T, Bathe KJ. A finite element formulation for nonlinear incompressible elastic and inelastic analysis. *Computers & Structures* 1987; **26**(1):357–409.
30. Atluri SN, Reissner E. On the formulation of variational theorems involving volume constraints. *Computational Mechanics* 1989; **5**(5):337–344.
31. Herrmann LR. Elasticity equations for incompressible and nearly incompressible materials by a variational theorem. *AIAA Journal* 1965; **3**(10):1896–1900.
32. Ogden RW. Volume changes associated with the deformation of rubber-like solids. *Journal of the Mechanics and Physics of Solids* 1976; **24**(6):323–338.
33. Ogden RW. Nearly isochoric elastic deformations: application to rubberlike solids. *Journal of the Mechanics and Physics of Solids* 1978; **26**(1):37–57.
34. Arroyo M, Ortiz M. Local maximum-entropy approximation schemes: a seamless bridge between finite elements and meshfree methods. *International Journal for Numerical Methods in Engineering* 2006; **65**(13):2167–2202.
35. Belikov VV, Ivanov VD, Kontorovich VK, Korytnik SA, Semenov AY. The non-Sibsonian interpolation: a new method of interpolation of the values of a function on an arbitrary set of points. *Computational Mathematics and Mathematical Physics* 1997; **37**(1):9–15.
36. Floater MS, Hormann K, Kös G. A general construction of barycentric coordinates over convex polygons. *Advances in Computational Mathematics* 2004; **24**(1-4):311–331.
37. Hiyoshi H, Sugihara K. Two generalizations of an interpolant based on Voronoi diagrams. *International Journal of Shape Modeling* 1999; **5**(2):219–231.

38. Joshi P, Meyer M, DeRose T, Green B, Sanocki T. Harmonic coordinates for character articulation. *ACM Transactions on Graphics (TOG)* 2007; **26**(3):Article 71.
39. Malsch EA, Lin JJ, Dasgupta G. Smooth two dimensional interpolants: a recipe for all polygons. *Journal of Graphics Tools* 2005; **10**(2):27–39.
40. Meyer M, Barr A, Lee H, Desbrun M. Generalized barycentric coordinates on irregular polygons. *Journal of Graphics Tools* 2002; **7**:13–22.
41. Sukumar N. Construction of polygonal interpolants: a maximum entropy approach. *International Journal of Numerical Methods in Engineering* 2004; **61**(12):2159–2181.
42. Floater MS. Mean value coordinates. *Computer Aided Geometric Design* 2003; **20**(1):19–27.
43. Talischi C, Paulino GH. Addressing integration error for polygonal finite elements through polynomial projections: a patch test connection. *Mathematical Models and Methods in Applied Sciences* 2014; **24**(8):1701–1721.
44. Cook RD, Malkus DS, Plesha ME, Witt RJ. *Concepts and Applications of Finite Element Analysis* (4th edn). John Wiley & Sons, Ltd.: New York, 2002.
45. Lopez-Pamies O, Goudarzi T, Danas K. The nonlinear elastic response of suspensions of rigid inclusions in rubber: II — a simple explicit approximation for finite-concentration suspensions. *Journal of the Mechanics and Physics of Solids* 2013; **61**:19–37.
46. Lopez-Pamies O. An exact result for the macroscopic response of particle-reinforced Neo-Hookean solids. *Journal of Applied Mechanics* 2010; **77**(2):021016.
47. Lopez-Pamies O, Idiart MI, Nakamura T. Cavitation in elastomeric solids: I — A defect growth theory. *Journal of the Mechanics and Physics of Solids* 2011; **59**:1464–1487.
48. Gent AN. Cavitation in rubber: a cautionary tale. *Rubber Chemistry and Technology* 1990; **63**(3):49–53.
49. Nakamura T, Lopez-Pamies O. A finite element approach to study cavitation instabilities in non-linear elastic solids under general loading conditions. *International Journal of Non-Linear Mechanics* 2012; **47**(2):331–340.
50. Xu X, Henao D. An efficient numerical method for cavitation in nonlinear elasticity. *Mathematical Models and Methods in Applied Sciences* 2011; **21**(08):1733–1760.
51. Lopez-Pamies O. A new I_1 -based hyperelastic model for rubber elastic materials. *Comptes Rendus Mecanique* 2010; **338**(1):3–11.
52. Ball JM. Discontinuous equilibrium solutions and cavitation in nonlinear elasticity. *Philosophical Transactions of the Royal Society of London. Series A, Mathematical and Physical Sciences* 1982; **306**(1496):557–611.